RSC Advances

PAPER

View Article Online
View Journal | View Issue

Cite this: *RSC Adv.*, 2026, **16**, 22587

Reactive sputtered Zn_3N_2–CN_x hybrid films for silicon heterojunction photodetection

Ali J. Addie, *[a] Raid A. Ismail, [b] Azhar I. Hassan [b] and Mudhafar A. Mohammed[b]

Nanohybrid semiconductors comprising distinct nanoscale components offer new opportunities for tailored optoelectronic properties. In this work, Zn_3N_2–CN_x hybrid thin films were prepared by reactive RF magnetron sputtering from a segmented Zn/graphite target and used to fabricate p-Si heterojunction photodetectors. The hybrid-film approach was explored as a route to modify the electronic character of a Zn_3N_2-rich sputtered overlayer and its junction response on silicon. X-ray diffraction and microscopy indicated a heterogeneous nanostructured film, Raman spectroscopy showed retention of a CN_x-like disordered carbon-nitride network, and elemental mapping confirmed spatial coexistence of Zn, N, and C with a measurable O contribution in the as-deposited layer. Optical analysis revealed characteristic energies associated with the Zn_3N_2-rich and CN_x-containing components. The Zn_3N_2–CN_x/p-Si heterojunction exhibited an ideality factor of ~2.9, a rectification ratio of ~13.7 at 5 V, a maximum responsivity of ~0.40 A W^{-1} at 550 nm, and a detectivity of ~2.03 × 10^{11} Jones, together with stable transient switching and rise/recovery times of ~0.5/0.7 ms. The results support the formation of an electronically distinct hybrid overlayer whose incorporation is associated with improved heterojunction photodetection on p-Si. Reactively sputtered Zn_3N_2–CN_x therefore represents a promising hybrid thin-film platform for Si-based optoelectronic devices.

Received 23rd March 2026
Accepted 25th April 2026

DOI: 10.1039/d6ra02403c

rsc.li/rsc-advances

1. Introduction

Silicon remains the most scalable and technologically mature platform for photodetectors because it combines wafer-level manufacturability, process compatibility, and low-cost integration with established microelectronic fabrication. In modern Si heterojunction photodetectors, however, device performance is increasingly limited by the buried interface rather than by the Si substrate itself. Recent reviews and benchmark studies on low-dimensional, mixed-dimensional, and 2D/Si photodetectors show that, once silicon provides the transport backbone, further gains in responsivity, detectivity, dark-current suppression, and bias efficiency depend mainly on band alignment, interfacial trap density, depletion-field control, and junction selectivity.[1–4] This trend is evident in recent device reports, where performance improvements were achieved by tunneling-oxide passivation in Bi_2O_2Se/Si junctions,[5] narrow-bandgap Te/Si photodiodes,[6] graphene/Si architectures with interface-tailored barrier transport,[7] and interface-engineered PEDOT:PSS/Si hybrid junctions.[8] These studies establish a clear criterion for new Si heterojunction architectures: the partner layer must do more than extend absorption; it must also reshape junction electrostatics and interfacial defect physics.

Hybrid thin films are attractive because they can integrate multiple interface-relevant functions into a single deposited layer, including carrier-density modulation, defect redistribution, transport selectivity, and local field shaping. Recent reviews and benchmark device studies frame hybridization not as simple compositional mixing, but as a route to engineering interfacial energetics and recombination pathways that are difficult to realize in single-component films.[9–12] More generally, the development of photodetectors based on low-dimensional layered materials, graphene/semiconductor hybrid heterostructures, and other interface-engineered Si platforms has established that the principal advantage of hybridization lies not merely in broadened absorption, but in its ability to modify carrier separation, transport selectivity, and junction electrostatics.[13–15] This is especially important in photodetectors, where hybrid or mixed-dimensional systems become compelling only when the secondary phase produces a measurable electronic effect at the interface, rather than merely altering morphology.[3,4,9–12] The present work therefore examines whether a sputtered Zn_3N_2–CN_x hybrid overlayer can function as a more electronically selective and less defect-active junction partner for p-Si.

Among earth-abundant nitride semiconductors, Zn_3N_2 is a promising but under-controlled candidate for this role. It is attractive because it can be deposited by scalable physical-vapor routes, exhibits substantial visible-light absorption, and generally shows n-type transport relevant to heterojunction

[a]*Center of Industrial Applications and Materials Technology, Scientific Research Commission, Baghdad, Iraq. E-mail: ali.jaddie@yahoo.com*
[b]*College of Applied Science, University of Technology-Iraq, Baghdad, Iraq*

formation.[16–20] However, Zn_3N_2 rarely behaves as an electronically simple semiconductor. Its reported optical gap varies widely across the literature, and this spread is now linked to carrier-induced Burstein–Moss shifts, point defects, and oxygen-related chemistry.[21,22] More recent work has shown that oxygen is not merely incidental contamination, but can drive Zn_3N_2 away from the strongly degenerate regime and substantially alter resistivity, carrier density, and optical response.[18] As a result, experimentally realized Zn_3N_2 films are often characterized by electron concentrations in the 10^{19}–10^{21} cm^{-3} range,[17,18,23] which is unfavorable for photodetector junctions because excessive free-carrier density can suppress depletion, increase leakage, and weaken electrostatic selectivity. In addition, Zn_3N_2 is chemically unstable under ambient oxygen exposure, and oxidation can modify its electronic properties even when oxide-related signatures are not obvious in XRD.[18,22,24,25] Thus, although Zn_3N_2 is electronically active, its standalone thin-film form remains insufficiently controlled for reliable interface engineering.

Carbon nitride thin films (CN_x) offer a complementary set of attributes, combining chemical stability, broad processing flexibility, and electronically tunable bonding disorder. Recent work on amorphous CN_x and graphitic/polymeric carbon nitride films has shown that carbon nitride can be deposited directly on technologically relevant substrates, including Si, by sputtering and vapor-phase routes.[26–30] This has expanded carbon nitride from a mainly photocatalytic material toward a more device-oriented thin-film platform, as illustrated by rapid CVD growth of graphitic carbon nitride films,[27] controlled growth of ultrathin graphitic carbon nitride films,[28] and ultrathin amorphous carbon nitride integrated with Si vertical photodiodes, where the carbon nitride layer acted as an electronically active junction partner rather than a passive coating.[29] However, CN_x is not electronically ideal in isolation. Its bonding structure is strongly preparation-dependent, and sputtered or amorphous CN_x films can contain variable mixtures of sp^2-rich carbon environments, C–N/C=N motifs, structural disorder, and depth-dependent composition.[26,31] Recent analyses further show that carbon-nitride thin-film functionality is strongly dependent on bonding topology, defect structure, film continuity, and interface construction.[32–34] CN_x is therefore relevant here not as a complete standalone device material, but as a highly perturbable carbon-nitride network that may modify interfacial charge transfer and defect response in a hybrid film.

The integration of Zn_3N_2 with CN_x arises from the complementary electronic roles of the two phases. Zn_3N_2 serves as an electronically active nitride-rich matrix, but its device performance is limited by excess carrier density and oxygen-sensitive defect chemistry. CN_x, by contrast, provides a carbon-nitride-rich network whose local bonding structure and transport behavior are readily altered by growth conditions and interphase coupling. These characteristics become complementary at the heterojunction: the Zn_3N_2-rich phase sustains conductivity and visible-light activity, while the CN_x-rich phase can regulate carrier density, trap response, and charge-transfer processes without dominating the overall film composition. This view is consistent with a broader trend in photodetector research, where secondary phases are valuable only when they produce a measurable electronic effect at the interface.[3,4,9–12] It is also consistent with recent carbon nitride/Si and interface-engineered Si device studies showing that modest changes in interface quality can lead to substantial changes in dark current, responsivity, and detectivity.[5–8,29]

In this work, Zn_3N_2–CN_x hybrid thin films were deposited by reactive RF magnetron sputtering from a segmented Zn/graphite target and integrated into p-Si heterojunction photodetectors. The work examines the effect of introducing a CN_x-containing secondary network into a Zn_3N_2-rich sputtered film on the structural, electronic, and junction properties of the resulting heterostructure relative to a Zn_3N_2 reference. The scope is focused on hybrid-film formation, compositional coexistence, and the role of the hybrid overlayer as an electronically active partner in Si-based photodetection. Under this framework, the Zn_3N_2–CN_x layer is treated as a sputtered hybrid platform in which CN_x incorporation is linked to modified carrier transport and improved heterojunction behavior on p-Si.

2. Experimental and characterization techniques

2.1. Deposition of Zn_3N_2–CN_x hybrid thin films

Zn_3N_2–CN_x hybrid thin films were deposited on soda-lime glass and p-type silicon substrates using a NanoSys500 ultra-high-vacuum multi-PVD system (Mantis Deposition Ltd, UK). The deposition chamber was evacuated to a base pressure below 1×10^{-7} mbar prior to sputtering. Film growth was carried out by reactive RF magnetron sputtering from a mosaic target consisting of Zn and graphite segments. Depositions were performed at a constant working pressure of 1×10^{-3} mbar in an N_2/Ar atmosphere with flow rates of 27 and 3 sccm, respectively. The applied RF power was 50 W, corresponding to a power density of ~2.55 W cm^{-2}, and the target-to-substrate distance was 15 cm. Substrates were rotated continuously at 5 rpm during deposition to promote film uniformity, and the deposition time was fixed at 30 min for all samples. The relative fraction of Zn_3N_2 and CN_x in the deposited films was controlled by the area ratio of the Zn and graphite segments in the mosaic target, as described in previous work.[35]

2.2. Thin-film characterization

The optical transmission and reflectance of the prepared thin films on glass and silicon substrates were measured by a UV/Vis-NIR double beam spectrophotometer (V-670, JASCO, Japan). The spectrophotometer has a wavelength range of (300–1200 nm). X-ray diffraction measurements were performed using a Shimadzu LabX XRD-6000 system, Japan, with a 2 kW Cu-Kα radiation (λ = 1.5405 Å). The scanning angle ranges over 2θ from 10° to 80° with a minimum step angle of 0.002° (2θ). Surface morphology were investigated by a Zeiss Sigma 300 FESEM equipped with an X-ray energy dispersive spectroscopy detector. Raman spectra were measured using a confocal Raman microscope (Senterra, Bruker Optics, Germany) with 532 nm excitation laser sources. Spectra acquisition was

performed over the range 50–4400 cm^{-1} with various laser powers and integration times on each point. Atomic force microscopy was done using a multi-mode AFM (Ntegra, NT-MDT, Russia) operating in tapping non-contact mode with an Etalon tip.

2.3. Device fabrication

The p-type Si(100) substrates were immersed in diluted HF for approximately 4 min immediately prior to deposition to remove the native oxide layer. Both glass and silicon substrates were then ultrasonically cleaned in organic solvents, rinsed sequentially with ethanol, acetone, and deionized water, and dried under nitrogen flow. Ultra-flat stealth-diced p-Si dies (10 × 10 mm, 10–20 Ω cm; Ted Pella Inc.) were selected to minimize edge damage and debris associated with conventional saw dicing. Aluminum contacts were deposited by thermal evaporation through a shadow mask in the same PVD chamber at a base pressure of 10^{-6} mbar and a deposition rate of ∼1.0 Å s^{-1}. A thin Au coating (∼30 nm) was also applied to the backside of the Si substrate in order to promote a stable, low-resistance back contact during device characterization.

2.4. Device characterization

The electrical and photoelectric performance of the heterojunction devices was evaluated using an integrated Sciencetech PTS-2-QE Quantum Efficiency System (Sciencetech Inc., Canada). Current–voltage (*I–V*) characteristics were measured inside a light-tight sample chamber using the system's internal Keithley 2450 source-measure unit (SMU). Dark-current measurements were used to determine the saturation current and ideality factor (n) from the semi-logarithmic *I–V* plots. The rectification factor (RF) was calculated as the ratio of the forward to reverse current at an applied bias of 5 V.

Hall-effect measurements were carried out using a MeasureReady™ FastHall™ Station (Lake Shore Cryotronics, USA) to evaluate the electrical transport properties of the deposited films. The measurements were used to determine the Hall coefficient, carrier type, carrier concentration, mobility, and resistivity/sheet resistance of the films. Data acquisition and analysis were performed using the integrated M91 FastHall™ measurement controller and MeasureLINK™-MCS software platform. The Hall measurements provided direct information on the transport behavior of the hybrid films and were used to correlate the film conductivity with the heterojunction device performance.

Photoresponse characterization was performed under white-light illumination provided by a 150 W xenon short-arc lamp. Illuminated *I–V* curves were recorded over the voltage range from −10 to +10 V with a step of 0.1 V. The spectral responsivity (R) and external quantum efficiency (EQE/IPCE) were measured in the wavelength range of 300–900 nm using a 1/4 m Czerny–Turner monochromator equipped with a motorized triple-grating turret and automated order-sorting filters. During spectral scanning, the monochromatic probe beam was modulated with an optical chopper operated in the range of 10–200 Hz, and the resulting photocurrent was detected using a Stanford Research Systems SR800 series lock-in amplifier to improve the signal-to-noise ratio. All measurements and data acquisition were controlled through the SciPV software platform.

3. Results and discussions

The Results and discussion section begins with the characterization of films deposited under the optimized growth conditions. The hybrid films were prepared by RF magnetron sputtering from the mosaic target using 27 sccm N_2 and 3 sccm Ar at 50 W for 30 min. This power was selected as the highest stable operating value for the mosaic target without plasma breakdown and enabled co-deposition of both components.

Fig. 1a and b presents the FESEM images of the deposited films at high and low magnifications, respectively. The surface morphology is generally similar to that of Zn_3N_2 films prepared under comparable conditions, indicating that Zn sputtering remains dominant during deposition, consistent with the expected sputtering yields of Zn and C. The low-magnification image in Fig. 1b confirms that the film covers the surface uniformly, whereas the high-magnification image in Fig. 1a reveals a granular morphology with a stronger tendency toward cluster-like agglomeration than the more separated grains observed previously.

The grain-size distribution shown in Fig. 1d yields an average grain size slightly larger than that previously obtained for films deposited using pure Zn or pure graphite targets. In addition, the distribution can be deconvoluted into two overlapping normal components centered at approximately 28 and 10 nm, indicating the presence of two characteristic grain populations on the surface. Such bimodal behavior is consistent with the hybrid nature of the deposited film, where the smaller-size population may plausibly be associated with the CN_x-rich component, while the larger-size population is more likely related to the Zn_3N_2-rich grains. Accordingly, the bimodal grain-size distribution is interpreted not as stand-alone proof of phase separation, but rather as part of a convergent set of structural, compositional, and spectroscopic observations consistent with a Zn_3N_2-dominant hybrid film containing a CN_x-rich component.

Atomic force microscopy was used to further examine the surface morphology and topography of the hybrid film deposited on the silicon substrate. As shown in Fig. 2, the 1 × 1 μm^2 AFM scan provides the surface morphology in Fig. 2a, while the corresponding grain-size distribution and three-dimensional topography are presented in Fig. 2b. The film exhibits a cauliflower-like surface composed of agglomerated nanoscale granular clusters, in good agreement with the FESEM observations. The AFM grain-size analysis gives an average value of about 31 nm, which is slightly larger than that obtained from SEM. This difference is expected because AFM lateral dimensions are often overestimated due to tip-convolution effects during scanning. In contrast to the SEM grain-size distribution, no clear overlapping distribution was resolved in the AFM data, which may be related to the limited scan area and the lower statistical representation of the smaller clusters.

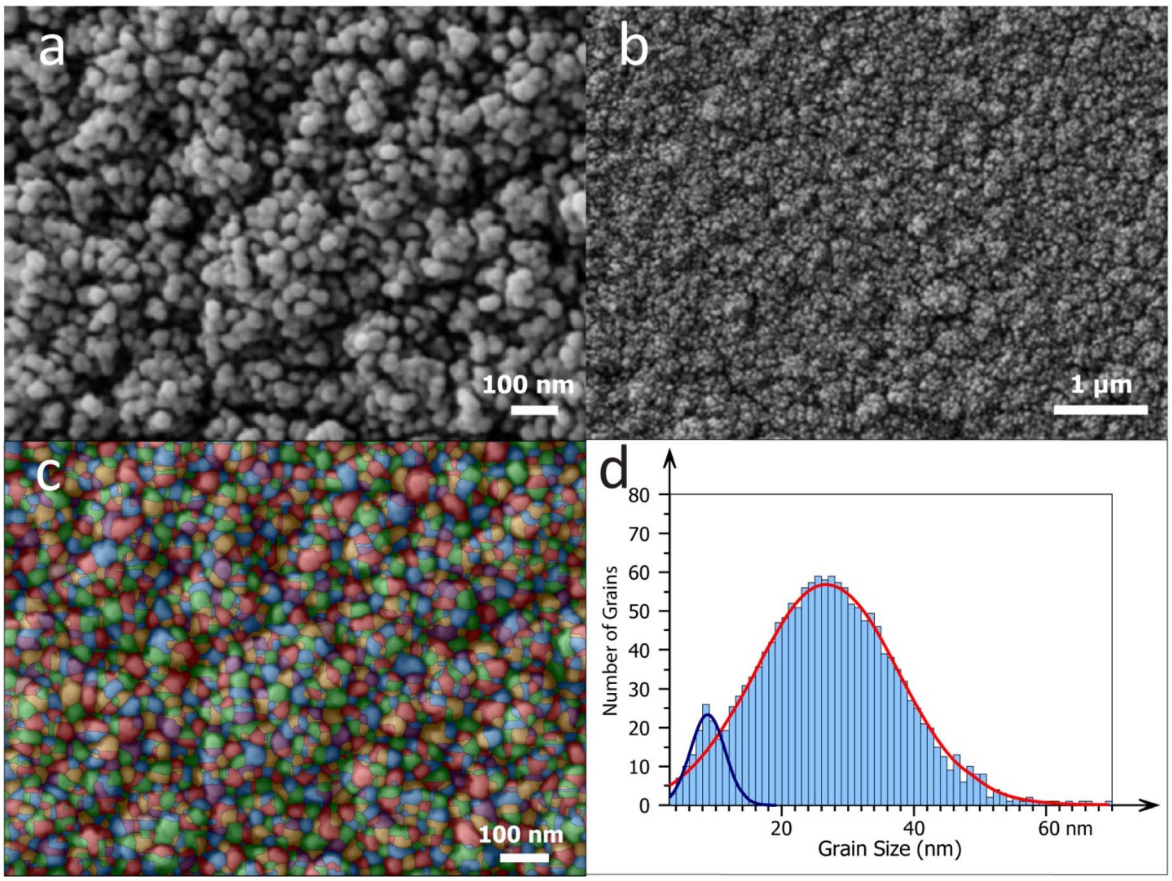

Fig. 1 FESEM of the Zn–N–C hybrid films on the silicon substrate: (a) high magnification image with 100 nm scale, (b) low magnification image with 1 μm scale, (c) image segmentation based on watershed edge detection method, and (d) grain size distribution histogram and normal distribution curve.

In addition to topography, AFM phase-contrast imaging can provide qualitative information about surface heterogeneity and possible variations in local composition or mechanical response.[36,37] Fig. 2c and d shows the topography and phase images acquired simultaneously from the same scanned area. The phase image in Fig. 2d reveals regions of contrast distributed across and between the grains, indicating local differences in material properties. Since the cantilever response is influenced by variations in adhesion, stiffness, and viscoelastic behavior, these phase shifts suggest the presence of more than one surface environment. The small regions marked by white circles exhibit a contrast distinct from the surrounding matrix, which may indicate clusters with properties different from the dominant phase. Considering the hybrid nature of the deposited film, these regions may be associated with the CN_x-rich component, although phase-contrast imaging alone does not provide definitive phase identification.

To further evaluate the surface relief of the hybrid film, a height-profile analysis was extracted from the 1×1 μm^2 AFM image, as shown in Fig. 3. The profile reveals a corrugated surface composed of coalesced nanoscale features that form cluster-like surface domains separated by shallow valleys. The dotted vertical lines mark the lateral extent of a representative cluster, indicating that the observed morphology is governed not only by individual grains but also by their aggregation into larger topographic units. This observation is consistent with the cauliflower-like morphology identified in the FESEM and AFM images.

The roughness parameters derived from the AFM analysis are summarized in the inset of Fig. 3. The film exhibits root-mean-square roughness (R_q) and arithmetic average roughness (R_a) values of 16.51 and 13.28 nm, respectively, indicating a moderately rough surface with relatively uniform height variations. The limited difference between R_q and R_a suggests that the height distribution is not dominated by isolated extreme asperities, but rather by broadly distributed surface undulations associated with the clustered morphology. The skewness value ($R_{sk} = -0.2156$) is slightly negative, which indicates a mild tendency toward valley-dominated topography, while the kurtosis value ($R_{ku} = 2.815$), being close to 3, suggests a near-normal height distribution with rounded rather than sharply peaked surface features. Overall, the line-profile analysis supports the formation of a clustered and topographically heterogeneous surface, while still preserving a relatively regular vertical roughness distribution.

Thin-film growth in sputtering systems is governed by the interaction between the substrate surface and the atoms, radicals, and clusters arriving from the plasma phase. In the present

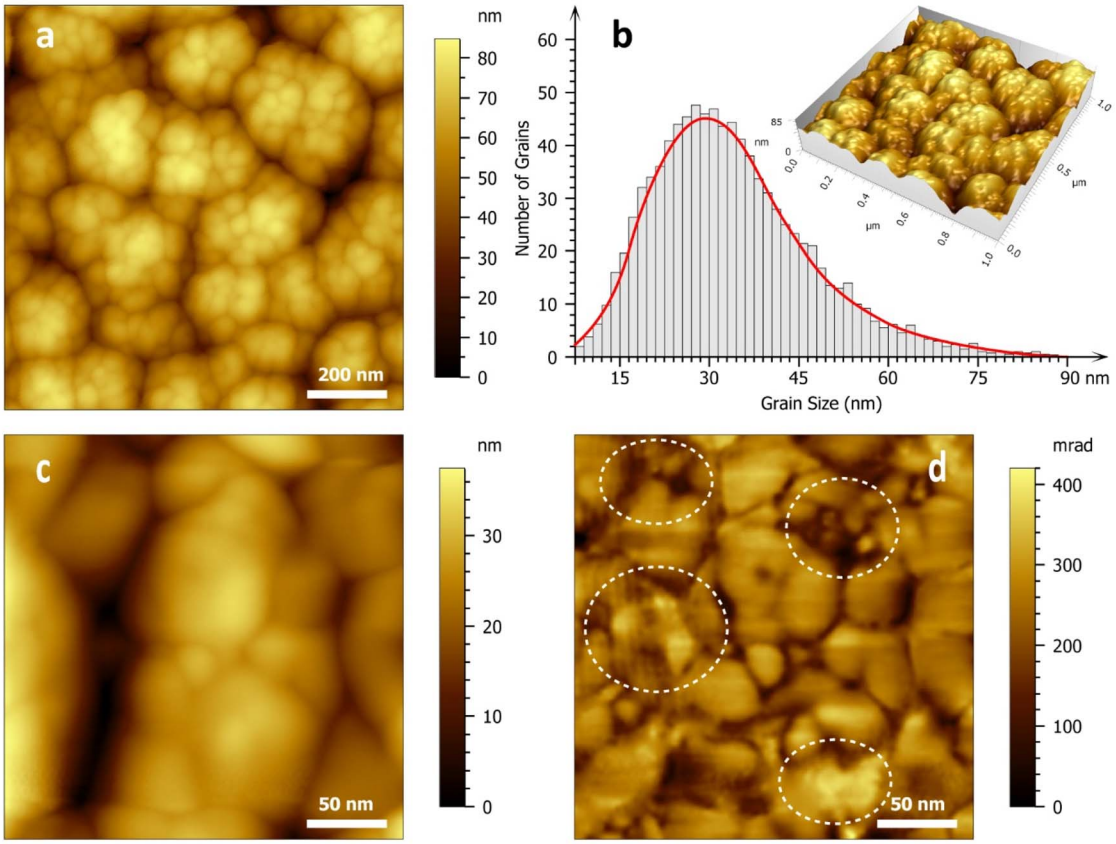

Fig. 2 Atomic force microscopy of the hybrid nitride system with a scan area of 1 × 1 μm^2. (a) 2D surface topography and (b) grain size distribution histogram and normal distribution curve with 3D image inset. (c) High-resolution atomic force microscope images (scan area of 250 × 250 nm^2). (c) Image of AFM topography mode and (d) image of AFM phase-contrast mode.

case, the cauliflower-like morphology and clustered surface evolution suggest that the film growth cannot be described adequately by a purely diffusion-controlled mechanism. Rather, the theory of charged clusters (TCC) provides a more suitable framework for interpreting the growth behavior.[38,39] Within this model, nanoscale clusters nucleate and grow in the gas phase prior to deposition, and the final microstructure develops through their subsequent interaction with the substrate surface. Plasma-generated electrons and ions can impart charge to these clusters, while cluster coalescence may occur before charging. Once charged, however, further agglomeration is hindered by coulombic repulsion, which limits the cluster size and affects the structural arrangement of the deposited layer.[39,40] This interpretation is consistent with the structural

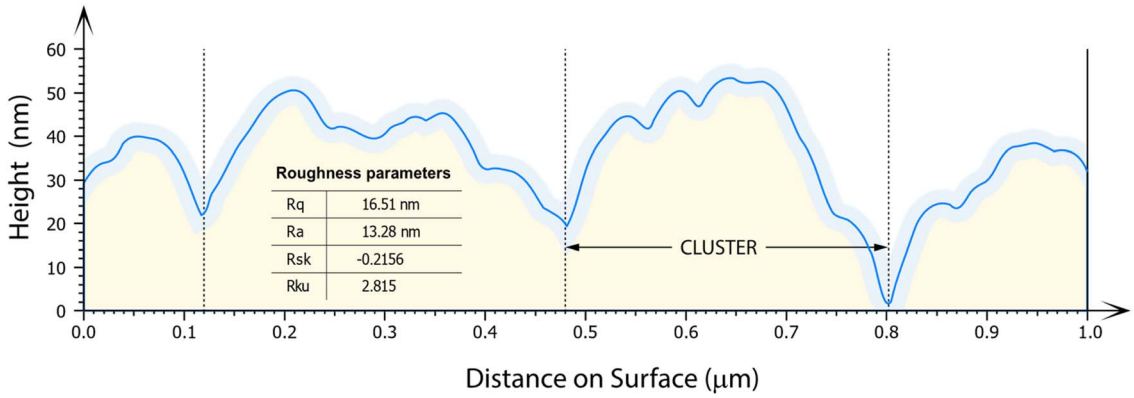

Fig. 3 AFM height profile extracted from the 1 × 1 μm^2 image of the hybrid film surface, together with the corresponding roughness parameters. The dotted lines indicate the lateral extent of a representative surface cluster.

features observed in Fig. 4a. The XRD pattern of the hybrid film shows weak and broadened reflections at positions corresponding to indexed Zn_3N_2 planes, as indicated in the figure, superimposed on a broad diffuse background and a broad feature in the low-angle region characteristic of disordered carbon-based material. The indexed reflections were assigned by comparison with the standard Zn_3N_2 reference pattern (ICDD card no. 35-0762). Together, these features indicate that the hybrid layer is predominantly poorly crystallized, consisting of a Zn_3N_2-rich phase embedded within a structurally disordered carbon-nitride-containing matrix.

In this hybrid system, the effect of thermal treatment is expected to be multifaceted, because annealing may influence not only crystallinity and defect density but also oxygen-related chemistry and the relative balance between the Zn_3N_2-rich and CN_x-containing components. For this reason, controlled annealing under suitable atmospheres represents a potentially valuable route for further optimization of film quality and heterojunction performance in future work.

The compositional features of the hybrid film are further supported by the EDS spectrum and elemental maps shown in Fig. 4b. Across five randomly selected surface regions, the film exhibited an average composition of 75.5 ± 1.8 wt% Zn, 12.9 ± 1.0 wt% C, 7.7 ± 0.8 wt% N, and 3.9 ± 0.6 wt% O. When expressed in normalized atomic proportions, this corresponds approximately to Zn : C : N : O = 1.00 : 0.93 ± 0.08 : 0.48 ± 0.05 : 0.21 ± 0.03. The relatively small standard deviations indicate good micrometer-scale compositional reproducibility. The film is clearly Zn-rich, whereas the reduced nitrogen content is consistent with the known tendency of reactively sputtered zinc nitride films to deviate from ideal stoichiometry under practical growth conditions.[18,19] The elemental maps further show that Zn, N, and C are laterally distributed across the scanned region without evidence of gross micron-scale segregation, supporting the formation of a hybrid Zn_3N_2–CN_x layer rather than a mere spatial superposition of isolated nitride-rich and carbon-rich domains. A reproducible oxygen signal was also detected across multiple analyzed regions, confirming that oxygen is an intrinsic part of the as-deposited film chemistry rather than an analytical artifact. However, because the present EDS analysis is not depth-resolved, it does not permit determination of whether the oxygen is distributed uniformly through the film thickness or preferentially enriched near the surface or buried interface. This observation remains chemically important because oxygen

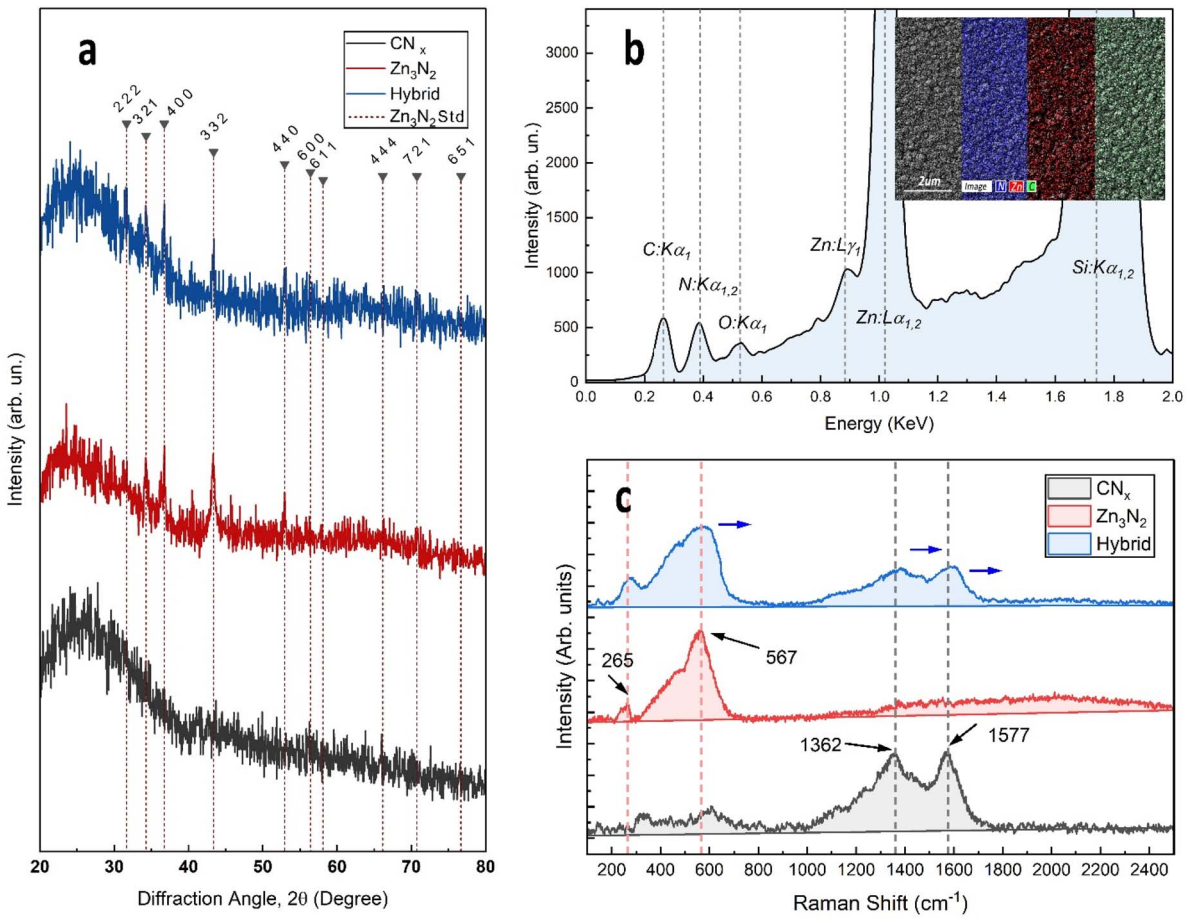

Fig. 4 (a) XRD patterns of CN_x, Zn_3N_2, and Zn_3N_2–CN_x thin films on glass; dashed lines and Miller indices indicate Zn_3N_2 reflections indexed using ICDD card no. 35-0762. (b) EDS spectrum and elemental mapping of the hybrid film. (c) Raman spectra of CN_x, Zn_3N_2, and Zn_3N_2–CN_x films.

incorporation and post-deposition oxidation are well documented in Zn_3N_2-based thin films and can significantly modify their structural and electronic behavior even when no distinct oxide phase is resolved by XRD.[18,19,25] Accordingly, the deposited layer is most appropriately described, at the compositional level probed here, as a Zn–N–C–O thin-film system with a Zn_3N_2-dominant character.

The Raman spectra of the CN_x, Zn_3N_2, and Zn_3N_2–CN_x films are presented in Fig. 4c. The CN_x reference film exhibits the broad D and G bands centered at approximately 1362 and 1577 cm^{-1}, respectively, with full widths at half maximum of about 198 cm^{-1} for the D band and 124 cm^{-1} for the G band, and an I_D/I_G ratio of approximately 0.96. These spectral features are characteristic of disordered carbon-nitride films under visible excitation, where the Raman response is dominated primarily by the disordered sp^2-bonded carbon network rather than by isolated C–N vibrational modes.[30,41–43] The broad line shape and moderate I_D/I_G value are therefore consistent with a sputtered CN_x phase containing defective aromatic clusters and substantial bond-angle and bond-length disorder. In contrast, the Zn_3N_2 reference film shows broad low-wavenumber bands at approximately 265 and 567 cm^{-1}, which can be assigned to Zn_3N_2-related vibrational modes,[44,45] while no pronounced D and G bands are observed.

For the Zn_3N_2–CN_x hybrid film, the Raman spectrum retains the characteristic carbon-related D and G bands, appearing at approximately 1359 and 1571 cm^{-1}, respectively, together with additional low-wavenumber features associated with the Zn_3N_2-rich component. Relative to the CN_x reference, the hybrid film exhibits a slight downshift and broadening of the G band, accompanied by a reduction in the I_D/I_G ratio to approximately 0.81. These changes indicate that the disordered CN_x-like sp^2 network is preserved in the hybrid layer but experiences a modified local bonding and electronic environment after coexistence with the Zn_3N_2-rich phase.[41–43] Within the Ferrari–Robertson framework, this behavior is more consistent with perturbation of the sp^2 cluster topology and disorder state than with the emergence of a new, independently resolved carbon phase. Therefore, the Raman results support hybrid-film formation by confirming retention of the CN_x-derived vibrational signature together with measurable spectral modification in the Zn_3N_2–CN_x layer. Although these data do not by themselves prove a specific Zn–N–C interfacial bond, when considered together with the XRD, EDS, and morphological observations they provide convergent evidence for a Zn_3N_2-dominant hybrid film containing a spectroscopically detectable carbon-nitride-rich component.

The optical transmittance spectrum of the as-deposited hybrid film on glass, recorded over the wavelength range of 300–1200 nm, is shown in Fig. 5a. The film exhibits low transmittance throughout most of the visible region, reaching only about 1.0% at 500 nm, and then increases progressively toward longer wavelengths to approximately 66% at 1200 nm. This behavior is similar to that of Zn_3N_2 films deposited under comparable conditions, although the hybrid film shows slightly higher transmittance in the visible range. The gradual transmittance variation, rather than a sharp absorption edge, is consistent with the hybrid and disordered character of the deposited layer. Unlike a well-crystallized single-phase semiconductor, the present film consists of a Zn_3N_2-rich component coexisting with a disordered CN_x-containing network, as supported by the weak and broadened XRD features and the broad Raman response of the carbon-nitride phase. In such a heterogeneous system, the optical edge is expected to be broadened by overlapping absorption contributions from the different components together with disorder-induced band-tail states and defect-related absorption associated with nonstoichiometry and oxygen incorporation. The observed transmittance behavior is therefore more appropriately interpreted as arising from a distribution of local electronic environments rather than from a single abrupt band-edge transition.[46]

Given that Zn_3N_2 is the dominant phase in the deposited layer, the optical transitions were analyzed using the Tauc relation, $\alpha h\nu = A(h\nu - E_g)^m$, where $m = 1/2$ for allowed direct transitions and $m = 2$ for allowed indirect transitions. From the linear extrapolation of $(\alpha h\nu)^2$ *versus* $h\nu$, shown in the inset of Fig. 5a, using the most nearly linear region in the range of approximately 2.3–3.1 eV, the apparent direct transition energy was estimated to be about 2.15 eV. This value is larger than that reported for single-crystal Zn_3N_2,[47] but remains comparable to values reported for reactively sputtered Zn_3N_2 thin films prepared under different growth conditions.[48–50] Likewise, extrapolation of $(\alpha h\nu)^{1/2}$ *versus* $h\nu$ over the approximately linear region of 1.1–2.2 eV gives an apparent indirect transition energy of about 0.96 eV, which can be associated with the CN_x-containing component of the hybrid film. Because the deposited layer is chemically and structurally heterogeneous, these values are more appropriately regarded as apparent optical transition energies rather than intrinsic bandgap values of isolated phases.

The slight modification of the optical transition behavior relative to the single-component films can be attributed to electronic interaction between the Zn_3N_2-rich matrix and the dispersed CN_x-rich phase. In such a hybrid system, the CN_x component may partially alter the local electronic environment of adjacent Zn_3N_2 domains, thereby affecting the absorption edge and the apparent transition energies extracted from the Tauc plots. This interpretation is consistent with the structural and spectroscopic results, which indicate a Zn_3N_2-dominant hybrid layer containing a disordered carbon-nitride-rich component.

Hall-effect measurements provide direct evidence that incorporation of CN_x modifies the transport properties of the Zn_3N_2-rich layer. Both the Zn_3N_2 reference film and the Zn_3N_2–CN_x hybrid film exhibited n-type conductivity. The pure Zn_3N_2 film showed an electron concentration of $(3.2 \pm 0.4) \times 10^{20}$ cm^{-3}, a Hall mobility of (4.6 ± 0.5) $cm^2\ V^{-1}\ s^{-1}$, and a resistivity of $(4.2 \pm 0.6) \times 10^{-3}$ Ω cm. By comparison, the Zn_3N_2–CN_x hybrid film exhibited a lower carrier concentration of $(6.8 \pm 0.9) \times 10^{19}$ cm^{-3}, a mobility of (3.1 ± 0.4) $cm^2\ V^{-1}\ s^{-1}$, and a higher resistivity of $(2.9 \pm 0.4) \times 10^{-2}$ Ω cm. The nearly one-order reduction in free-electron concentration, accompanied by only a moderate decrease in mobility, indicates that CN_x incorporation does not merely introduce additional disorder, but

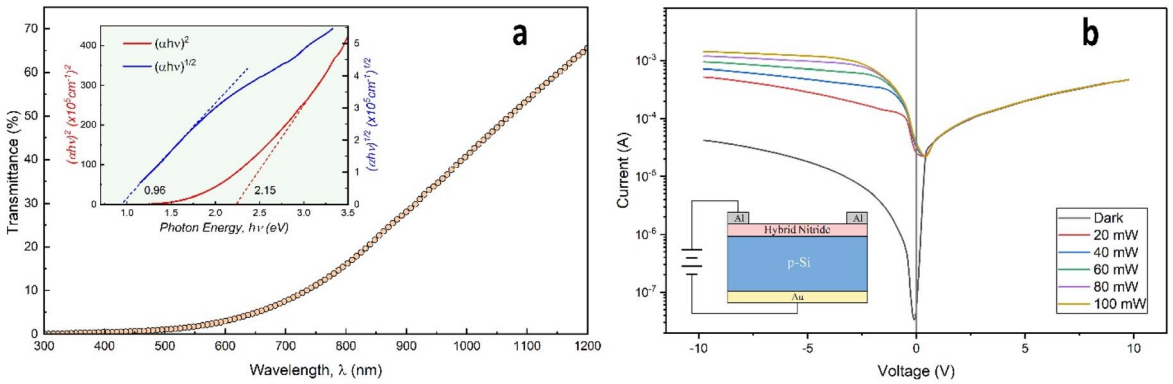

Fig. 5 (a) Optical transmittance of the film prepared from the mosaic target. The inset represents the linear fitting for the direct and indirect energy gap, and (b) semi-logarithmic plot of the dark and illuminated *I*–*V* characteristics of the heterojunction of the nanohybrid film on p-Si synthesized from the mosaic target.

instead shifts the Zn_3N_2-rich matrix toward a less strongly degenerate transport regime. This change is favorable for heterojunction formation on p-Si because it supports development of a more effective depletion region and is consistent with the improved rectification and photoresponse observed for the hybrid device.

The dark *C*–*V* characteristics support the same conclusion from the junction perspective. From the linear region of the $1/C^2$–*V* plots measured at 1 MHz, the built-in potential increased from 0.43 ± 0.03 V for the Zn_3N_2/p-Si junction to 0.61 ± 0.04 V for the Zn_3N_2–CN_x/p-Si junction. In parallel, the capacitance dispersion under reverse bias was reduced, for example from 24 ± 3% to 11 ± 2% between 10 kHz and 1 MHz at −1 V, while the interface-state density decreased from $(1.2 \pm 0.2) \times 10^{12}$ to $(4.6 \pm 0.7) \times 10^{11}$ cm^{-2} eV^{-1}. These results indicate that the hybrid heterointerface is electronically less defective and less dispersive than the Zn_3N_2/p-Si reference. Thus, the enhanced junction behavior is more directly explained by transport and interface modification than by morphology alone.

The semi-logarithmic dark and illuminated *I*–*V* characteristics of the Zn_3N_2–CN_x/p-Si heterojunction are presented in Fig. 5b. Under illumination, the photocurrent increases systematically with incident power, reflecting enhanced photogeneration and collection of electron–hole pairs. The ideality factor was determined from the linear forward-bias region using the diode relation $I = I_0 \exp(qV/nkT)$, and the device exhibited an ideality factor of about 2.9. This relatively large value indicates that the forward current is not governed by ideal thermionic emission alone. Instead, it is more plausibly associated with trap-assisted recombination through electrically active states at or near the heterointerface, together with a possible tunneling-assisted contribution through localized states in the disordered hybrid layer. In addition, some contribution from barrier inhomogeneity cannot be excluded. These factors are consistent with the non-ideal transport expected for a nanostructured Zn_3N_2–CN_x/p-Si heterojunction.[51] The rectification ratio, defined as $RR = I_F(+5\text{ V})/I_R(-5\text{ V})$, reached approximately 13.7, which is significantly higher than that obtained for the Zn_3N_2/p-Si heterojunction. This improvement indicates that the CN_x-containing hybrid layer modifies the excessive free-carrier character of Zn_3N_2 and promotes more effective junction formation with p-Si.

The increase in photocurrent with illumination intensity is not attributable to optical transmission alone, but rather to the combined influence of absorption, carrier generation, transport, and collection across the heterointerface. In the present system, the improved photoresponse of the hybrid device is more plausibly associated with the reduced carrier concentration of the Zn_3N_2-rich layer, the higher built-in potential, and the lower interface-state density indicated by the Hall and *C*–*V* analyses. At the same time, the clustered morphology and mixed-phase character of the film may facilitate local charge separation and transport across adjacent semiconducting domains. Accordingly, the enhanced photocurrent of the Zn_3N_2–CN_x/p-Si device is best understood as the result of coupled optical and electronic effects arising from hybridization, rather than from a single structural factor.

Fig. 6a illustrates the spectral responsivity (R_λ), external quantum efficiency (EQE), and specific detectivity (D^*) of the Zn_3N_2–CN_x/p-Si heterojunction measured under a reverse bias of 5 V. The spectral responsivity was determined from the photocurrent generated at each wavelength according to $R_\lambda = I_{ph}/P_{in} = (I_{light} - I_{dark})/(P_\lambda A)$, where I_{ph} is the photocurrent, P_{in} is the incident optical power on the illuminated area, P_λ is the monochromatic optical power density, and A is the effective illuminated device area.[52,53] The corresponding external quantum efficiency was calculated from the responsivity using $EQE = (R_\lambda hc)/(q\lambda)$, which, for λ expressed in nm, becomes $EQE\ (\%) = (1240R_\lambda/\lambda) \times 100$.[54] The specific detectivity was estimated using the shot-noise-limited expression $D^* = R_\lambda A^{1/2}/(2qI_d)^{1/2}$, where q is the elementary charge and I_d is the dark current at the corresponding bias.[55–57] Under reverse bias, the external electric field widens the depletion region and facilitates the separation and collection of the photogenerated electron–hole pairs, thereby suppressing recombination losses and enhancing the responsivity of the heterojunction. A broad spectral response was observed for the nanohybrid device, with the maximum shifted slightly relative to the pure Zn_3N_2 device. The

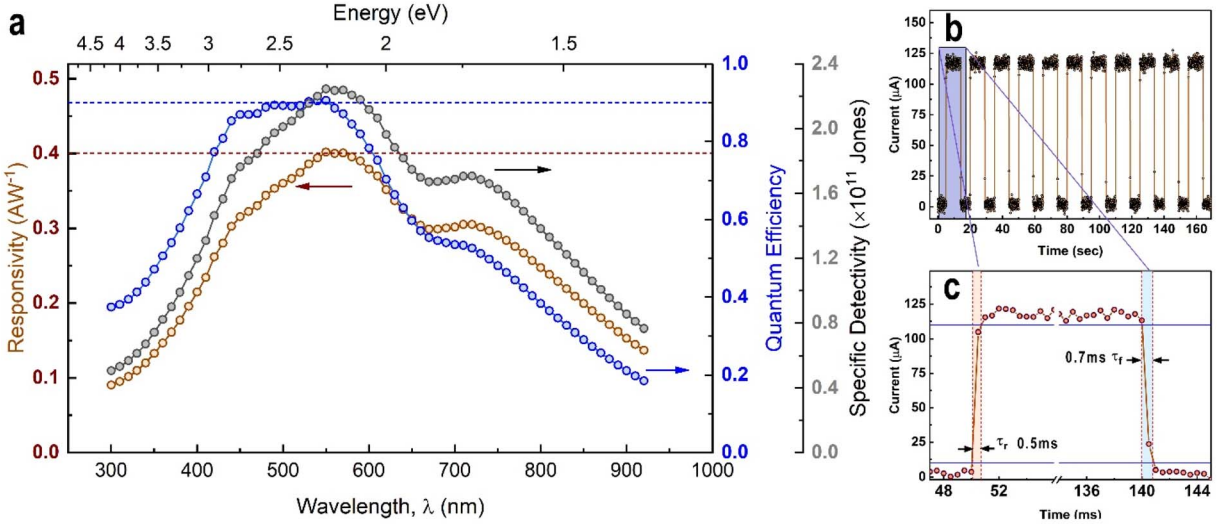

Fig. 6 (a) Spectral responsivity, external quantum efficiency, and specific detectivity of the Zn_3N_2–CN_x/p-Si heterojunction measured under a reverse bias of 5 V. (b) Time-dependent photocurrent response under periodic light on/off modulation. (c) Enlarged transient profile used to determine the rise time (τ_r) and fall time (τ_f).

peak responsivity reached 0.40 A W^{-1} at 550 nm, corresponding to an EQE of about 90%, which confirms efficient photocarrier generation and extraction in the visible region. The wavelength dependence of D^* followed the same general trend as R_λ, because detectivity increased with increasing responsivity and decreased with increasing dark-current contribution. Fig. 6b and c further presents the transient photoresponse of the Zn_3N_2–CN_x/p-Si heterojunction under periodic light on/off modulation. The device exhibits stable and repeatable switching between the dark and illuminated states over multiple cycles, indicating good reproducibility of the photocurrent response. From the enlarged transient profile in Fig. 6c, the rise time (τ_r) and fall time (τ_f) were estimated to be approximately 0.5 and 0.7 ms, respectively. These fast transient characteristics, together with the enhanced responsivity and detectivity, indicate that the Zn_3N_2–CN_x hybrid overlayer supports efficient carrier separation and transport at the heterojunction.

The responsivity maximum of the heterojunction was observed at 550 nm, indicating a slight shift relative to the pure Zn_3N_2 device. This shift can be related to the modified optical transition behavior of the hybrid nitride film, as inferred from the optical measurements. Compared with the pure nitride device, the hybrid heterojunction exhibited higher responsivity and higher EQE, reflecting improved photocarrier separation and collection at the hybrid-film/p-Si interface.

The spectral variation of the specific detectivity, D^*, followed the same general trend as the responsivity because both figures of merit are governed by the wavelength-dependent photocurrent, although D^* is also affected by the dark-current level. The maximum recorded detectivity was 2.03×10^{11} Jones at 550 nm. Based on the responsivity results reported in our previous work,[45] the corresponding best detectivity of the Zn_3N_2/p-Si device was about 8×10^9 Jones at 600 nm, showing that the hybrid device outperforms the Zn_3N_2 reference by nearly two orders of magnitude. The improvement is attributed to the combined effect of lower leakage current and higher spectral responsivity in the Zn_3N_2–CN_x/p-Si heterojunction. This behavior is also consistent with the higher optical transmittance of the hybrid film in the 300–900 nm range, which permits more photons to penetrate to the depletion region and participate in photocurrent generation, whereas the lower transmittance of the Zn_3N_2 film tends to confine absorption closer to the surface and results in reduced photocurrent output. Taken together, comparison with the Zn_3N_2/p-Si reference shows that CN_x incorporation improves the heterojunction through coupled transport, interfacial, and optical effects.

Table 1 Comparison of the present Zn_3N_2–CN_x/p-Si heterojunction photodetector with representative Si-based hybrid photodetectors reported in the literature

Device	Wavelength/range	Bias	R (A W^{-1})	D^* (Jones)	Ref.
Zn_3N_2–CN_x/p-Si	550 nm	5 V	0.40	2.03×10^{11}	**This work**
SnS_2/Si	340 nm	0 V	~3.8	~2×10^{14}	58
Chlorophyll-*b*/Si	435 nm	Self-bias	~0.73	~2.2×10^{12}	59
Ag/n-Si/Al_2O_3/CuS/ITO	980 nm	0 V	0.41	1.739×10^{11}	60
Bi_2O_3-decorated MWCNTs/n-Si	560 nm	6.5	1.37	8.5×10^{11}	61
Te/n-type Si	UV-vis-NIR	Self-powered	0.248	1.8×10^{12}	62
ZnO@$PdTe_2$/Si	254–1550 nm	0 V	1.23	1.56×10^{13}	12

Relative to the Zn_3N_2 film, the hybrid overlayer exhibits a lower free-electron concentration and higher resistivity, while the corresponding junction shows a higher built-in potential, lower interface-state density, improved rectification, higher responsivity, and markedly enhanced detectivity. These trends indicate that the performance improvement arises primarily from hybridization-induced transport modification and improved junction electrostatics, with the slightly higher optical transmittance of the hybrid layer likely providing an additional contribution to photocurrent generation.

Table 1 further places this result in context by showing that the Zn_3N_2–CN_x/p-Si heterojunction lies within the established performance window of Si-based hybrid/composite photodetectors: at 550 nm and 5 V reverse bias, its specific detectivity is comparable to some reported Si-based hybrid devices, higher than several lower-performing architectures, and lower than the best values reported for more extensively optimized self-powered mixed-dimensional systems.

4. Conclusions

Zn_3N_2–CN_x hybrid thin films were successfully deposited by reactive RF magnetron sputtering from a segmented Zn/graphite target and integrated into p-Si heterojunction photodetectors. Structural and morphological analyses indicate that the deposited layer is a Zn_3N_2-rich heterogeneous nanostructured film containing a retained CN_x-like disordered carbon-nitride network. FESEM and AFM reveal a clustered cauliflower-like surface with nanoscale granular features, while XRD, Raman spectroscopy, and EDS support the coexistence of Zn-, N-, and C-containing phases with a measurable oxygen contribution in the as-deposited layer. These results show that hybridization modifies not only film composition but also the nanostructural organization of the sputtered overlayer.

The electrical results further show that this hybridization is accompanied by a significant change in the electronic behavior of the Zn_3N_2-rich layer and of its junction with p-Si. Relative to the Zn_3N_2 reference, the hybrid film exhibits a lower electron concentration, while dark *C–V* analysis indicates a higher built-in potential and a reduced interface-state response. The Zn_3N_2–CN_x/p-Si device correspondingly shows improved rectification, a maximum responsivity of about 0.40 A W^{-1} at 550 nm, and a detectivity of about 2.03×10^{11} Jones. Taken together, the results indicate that the enhanced photodetector performance arises from the combined effect of hybrid-film nanostructure and improved junction electrostatics, with the electrical diagnostics providing the clearest evidence that CN_x incorporation modifies carrier transport and interfacial defect behavior. Accordingly, Zn_3N_2–CN_x represents a promising sputtered hybrid platform for Si-based photodetectors, and further evaluation of its behavior over extended ambient exposure times would be of interest, particularly to determine whether the CN_x-containing network contributes to moderating ambient-induced changes, although further progress will also require tighter control of composition, oxygen incorporation, and interface chemistry.

Author contributions

Ali J. Addie: conceptualization, methodology, investigation, formal analysis, data curation, visualization, writing – original draft, writing – review & editing. Raid A. Ismail: conceptualization, methodology, interpretation of results, writing – review & editing. Azhar I. Hassan: investigation, visualization, interpretation of results, writing – review & editing. Mudhafar A. Mohammed: formal analysis, visualization, interpretation of results, writing – review & editing. All authors discussed the results, contributed to the final form of the manuscript, and approved the submitted version.

Conflicts of interest

The authors declare that they have no conflict of interests.

Data availability

The datasets generated during and/or analyzed during the current study are available from the corresponding authors on reasonable request.

References

1 W. Tian, H. Sun, L. Chen, P. Wangyang, X. Chen, J. Xiong and L. Li, Low-Dimensional Nanomaterial/Si Heterostructure-Based Photodetectors, *InfoMat*, 2019, **1**(2), 140–163, DOI: 10.1002/inf2.12014.

2 D. Somvanshi and S. Jit, Advances in 2D Materials Based Mixed-Dimensional Heterostructures Photodetectors: Present Status and Challenges, *Mater. Sci. Semicond. Process.*, 2023, **164**, 107598, DOI: 10.1016/j.mssp.2023.107598.

3 K. Abbas, P. Ji, N. Ullah, S. Shafique, Z. Zhang, M. F. Ameer, S. Qin and S. Yang, Graphene Photodetectors Integrated with Silicon and Perovskite Quantum Dots, *Microsyst. Nanoeng.*, 2024, **10**(1), 81, DOI: 10.1038/s41378-024-00722-4.

4 X. Yang, Z. Liu, F. Gao, S. Zhang, H. Shang, Y. Hu, Y. Zhang, Z. Fu, Y. Huang, W. Feng and P. A. Hu, Mixed-Dimensional InSe–Si Heterojunction Nanostructures for Self-Powered Broadband Photodetectors, *ACS Appl. Nano Mater.*, 2021, **4**(12), 12932–12936, DOI: 10.1021/acsanm.1c03100.

5 T. P. Hung, W. H. Chen, Y. J. Chen, Y. H. Tu, Z. H. Huang, Y. L. Chueh, C. H. Yeh, C. W. Chen, Y. Y. Jhang, Y. H. Chu and C. Y. Chen, Ultrathin Bi2O2Se/Si Heterojunction Photodetector with Tunneling Oxide Passivation for Enhanced Optoelectronic Performance, *ACS Appl. Mater. Interfaces*, 2025, **17**(18), 26931–26939, DOI: 10.1021/acsami.5c03477.

6 B. Park, S. Beak, J. Yang, S. Hwang, J. D. Kwon, J. Yoon, S. Y. Kwon and Y. Kim, Tellurium/Silicon Based p–n Photodiode for near Infrared Heterostructure Photodetector Applications, *Appl. Surf. Sci.*, 2025, **687**, 162242, DOI: 10.1016/j.apsusc.2024.162242.

7 P. Ji, S. Yang, Y. Wang, K. Li, Y. Wang, H. Suo, Y. T. Woldu, X. Wang, F. Wang, L. Zhang and Z. Jiang, High-Performance

Photodetector Based on an Interface Engineering-Assisted Graphene/Silicon Schottky Junction, *Microsyst. Nanoeng.*, 2022, **8**(1), 9, DOI: 10.1038/s41378-021-00332-4.

8 Y. Fu, Y. Liu, K. Ma, Z. Ji, W. Mai and C. Zhao, Interfacial Engineering to Boost Photoresponse Performance and Stability of V2O5/n-Si Heterojunction Photodetectors, *J. Alloys Compd.*, 2020, **819**, 153063, DOI: 10.1016/j.jallcom.2019.153063.

9 A. Pelella, A. Grillo, E. Faella, G. Luongo, M. B. Askari and A. Di Bartolomeo, Graphene-Silicon Device for Visible and Infrared Photodetection, *ACS Appl. Mater. Interfaces*, 2021, **13**(40), 47895–47903, DOI: 10.1021/acsami.1c12050.

10 J. Cong, A. Khan, P. Hang, D. Yang and X. Yu, Graphene/Si Heterostructure with an Organic Interfacial Layer for a Self-Powered Photodetector with a High ON/OFF Ratio, *ACS Appl. Electron. Mater.*, 2022, **4**(4), 1715–1722, DOI: 10.1021/acsaelm.1c01350.

11 X. Xue, C. Ling, H. Ji, J. Wang, C. Wang, H. Lu and W. Liu, Self-Powered and Broadband Bismuth Oxyselenide/p-Silicon Heterojunction Photodetectors with Low Dark Current and Fast Response, *ACS Appl. Mater. Interfaces*, 2023, **15**(4), 5411–5419, DOI: 10.1021/acsami.2c15947.

12 T. Zhang, G. Wu, J. Wang, R. Du, H. Lin, Y. Ren and L. Tao, Self-Powered ZnO@PdTe 2/Si Heterojunction Photodetector with an Ultrafast Response for Color Imaging and Optical Communication, *ACS Appl. Mater. Interfaces*, 2024, **16**(26), 33819–33828, DOI: 10.1021/acsami.4c06233.

13 C. Xie, S. Liu, D. Ke, Y. Shan, H. Yu, C. Li, L. Yang, W. Yang and Z. Huang, Light Trapping Effect Enhanced Self-Filtered NIR Narrowband Light Sensors Featuring Asymmetric MXene Electrodes for Optical Communication, *IEEE Trans. Electron Devices*, 2025, **72**(6), 3050–3057, DOI: 10.1109/TED.2025.3564258.

14 C. Xie, C. Mak, X. Tao and F. Yan, Photodetectors Based on Two-Dimensional Layered Materials Beyond Graphene, *Adv. Funct. Mater.*, 2017, **27**(19), 1603886, DOI: 10.1002/adfm.201603886.

15 C. Xie, Y. Wang, Z.-X. Zhang, D. Wang and L.-B. Luo, Graphene/Semiconductor Hybrid Heterostructures for Optoelectronic Device Applications, *Nano Today*, 2018, **19**, 41–83, DOI: 10.1016/j.nantod.2018.02.009.

16 P. John, M. Al Khalfioui, C. Deparis, A. Welk, C. Lichtensteiger, R. Bachelet, G. Saint-Girons, H. Rotella, M. Hugues, M. Grundmann and J. Zúñiga-Pérez, Epitaxial Zn3N2thin Films by Molecular Beam Epitaxy: Structural, Electrical, and Optical Properties, *J. Appl. Phys.*, 2021, **130**(6), 65104, DOI: 10.1063/5.0057307.

17 Y. Wang, T. Ohsawa, Y. Kumagai, K. Harada, F. Oba and N. Ohashi, Achieving Non-Degenerate Zn3N2 Thin Films by near Room Temperature Sputtering Deposition, *Appl. Phys. Lett.*, 2019, **115**(9), 92104, DOI: 10.1063/1.5101037.

18 E. Sirotti, B. Scaparra, S. Böhm, F. Pantle, L. I. Wagner, F. Rauh, F. Munnik, C. M. Jiang, M. Kuhl, K. Müller, J. Eichhorn, V. Streibel and I. D. Sharp, Oxygen Incorporation as a Route to Nondegenerate Zinc Nitride Semiconductor Thin Films, *ACS Appl. Mater. Interfaces*, 2025, **17**(5), 7958–7968, DOI: 10.1021/acsami.4c16921.

19 A. Trapalis, J. Heffernan, I. Farrer, J. Sharman and A. Kean, Structural, Electrical, and Optical Characterization of as Grown and Oxidized Zinc Nitride Thin Films, *J. Appl. Phys.*, 2016, **120**(20), 205102, DOI: 10.1063/1.4968545.

20 X. Cao, A. Sato, Y. Ninomiya and N. Yamada, Oxygen-Doped Zinc Nitride as a High-Mobility Nitride-Based Semiconductor, *J. Phys. Chem. C*, 2015, **119**(10), 5327–5333, DOI: 10.1021/jp5122992.

21 Y. Kumagai, K. Harada, H. Akamatsu, K. Matsuzaki and F. Oba, Carrier-Induced Band-Gap Variation and Point Defects in Zn3 N2 from First Principles, *Phys. Rev. Appl.*, 2017, **8**(1), 14015, DOI: 10.1103/PhysRevApplied.8.014015.

22 L. Run, D. Ying, Y. Lin, G. Meng and H. Baibiao, Structural, Electronic, and Optical Properties of Oxygen Defects in Zn3N2, *J. Phys. Chem. B*, 2007, **111**(13), 3379–3383, DOI: 10.1021/jp0667902.

23 Y. Wang, T. Ohsawa, F. Alnjiman, J.-F. F. Pierson and N. Ohashi, Electrical Properties of Zinc Nitride and Zinc Tin Nitride Semiconductor Thin Films toward Photovoltaic Applications, *High Temp. Mater. Processes*, 2022, **41**(1), 343–352, DOI: 10.1515/htmp-2022-0028.

24 A. Trapalis, I. Farrer, K. Kennedy, A. Kean, J. Sharman and J. Heffernan, Improved Ambient Stability of Thermally Annealed Zinc Nitride Thin Films, *AIP Adv.*, 2020, **10**(3), 35018, DOI: 10.1063/1.5144054.

25 C. G. Núñez, J. L. Pau, M. J. Hernández, M. Cervera, E. Ruíz and J. Piqueras, Influence of Air Exposure on the Compositional Nature of Zn 3N 2 Thin Films, *Thin Solid Films*, 2012, **522**, 208–211, DOI: 10.1016/j.tsf.2012.07.002.

26 C. Jia, L. Yang, Y. Zhang, X. Zhang, K. Xiao, J. Xu and J. Liu, Graphitic Carbon Nitride Films: Emerging Paradigm for Versatile Applications, *ACS Appl. Mater. Interfaces*, 2020, **12**(48), 53571–53591, DOI: 10.1021/acsami.0c15159.

27 E. B. Chubenko, S. E. Maximov, C. D. Bui, V. T. Pham and V. E. Borisenko, Rapid Chemical Vapor Deposition of Graphitic Carbon Nitride Films, *Materialia*, 2023, **28**, 101724, DOI: 10.1016/j.mtla.2023.101724.

28 L. Chen, Q. Feng, P. Giusto, D. Luo, W. Zhang, J. Liu, M. Antonietti and K. Xiao, Controlled Growth of Ultrathin Graphitic Carbon Nitride Films by Chemical Vapor Deposition, *ACS Mater. Lett.*, 2025, **7**(3), 869–875, DOI: 10.1021/acsmaterialslett.4c02507.

29 H. Seung, J. Bok, J. S. Kim, J. Kim, H. Choi, J. Ahn, J. P. Hong, E. Yoon, S. Blumstengel, Y. Y. Kim, L. Colazzo, S. Park, D. K. Hwang, J. Park, C. Choi, T. Hyeon and D. H. Kim, Covalent Heterostructures of Ultrathin Amorphous Carbon Nitride and Si for High-Performance Vertical Photodiodes, *Nat. Synth.*, 2025, **4**(4), 514–522, DOI: 10.1038/s44160-024-00730-2.

30 A. J. Addie, R. A. Ismail and M. A. Mohammed, Amorphous Carbon Nitride Dual-Function Anti-Reflection Coating for Crystalline Silicon Solar Cells, *Sci. Rep.*, 2022, **12**(1), 9902, DOI: 10.1038/s41598-022-14078-0.

31 J. Zemek, J. Houdkova, P. Jiricek and T. Kocourek, Amorphous Carbon Nitride Films: Surface and Subsurface Composition and Bonding, *Langmuir*, 2024, **40**(37), 19538–19547, DOI: 10.1021/acs.langmuir.4c02007.

32 Z. Song, J. Hou, E. Raguin, A. Pedersen, E. O. Eren, E. Senokos, N. V. Tarakina, P. Giusto and M. Antonietti, Triazine-Based Graphitic Carbon Nitride Thin Film as a Homogeneous Interphase for Lithium Storage, *ACS Nano*, 2024, **18**(3), 2066–2076, DOI: 10.1021/acsnano.3c08771.

33 D. A. Acuña Leal, C. R. Santiago Ramírez, N. A. Ramos Delgado, S. Shaji and M. A. Gracia Pinilla, Graphitic Carbon Nitride Hybrid Thin Films for Energy Conversion: A Mini-Review on Defect Activation with Different Materials, *Nanotechnol. Rev.*, 2024, **13**(1), 20240127, DOI: 10.1515/ntrev-2024-0127.

34 Y. Li and H. Du, Engineering Graphitic Carbon Nitride for Next-Generation Photodetectors: A Mini Review, *RSC Adv.*, 2023, **13**(37), 25968–25977, DOI: 10.1039/d3ra04051h.

35 A. Addie, R. Ismail and M. Mohammed, 2D Particle-in-Cell/Monte Carlo Collision Simulation of Zn-C Mosaic Target Erosion, *J. Appl. Sci. Nanotechnol.*, 2022, **2**(4), 118–127, DOI: 10.53293/jasn.2022.5395.1185.

36 P. Eaton and P. West, Atomic Force Microscopy, *At. Force Microsc.*, 2010, **9780199570**, 1–256, DOI: 10.1093/acprof:oso/9780199570454.001.0001.

37 R. García, *Amplitude Modulation Atomic Force Microscopy*, Wiley-VCH Verlag GmbH & Co. KGaA, Weinheim, Germany, 2010.

38 H. M. Jang and N. M. Hwang, Theory of the Charged Cluster Formation in the Low Pressure Synthesis of Diamond: Part II. Free Energy Function and Thermodynamic Stability, *J. Mater. Res.*, 1998, **13**(12), 3536–3547, DOI: 10.1557/jmr.1998.0482.

39 N.-M. M. Hwang and D.-Y. Y. Kim, Charged Clusters in Thin Film Growth, *Int. Mater. Rev.*, 2004, **49**(3–4), 171–190, DOI: 10.1179/095066004225021891.

40 S. Sério, M. E. Melo Jorge, M. J. P. Maneira and Y. Nunes, Influence of O2 Partial Pressure on the Growth of Nanostructured Anatase Phase TiO2 Thin Films Prepared by DC Reactive Magnetron Sputtering, *Mater. Chem. Phys.*, 2011, **126**(1–2), 73–81, DOI: 10.1016/j.matchemphys.2010.12.008.

41 A. C. Ferrari, S. E. Rodil, J. Robertson, S. E. Rodil and J. Robertson, Interpretation of Infrared and Raman Spectra of Amorphous Carbon Nitrides, *Phys. Rev. B: Condens. Matter Mater. Phys.*, 2003, **67**(15), 155306, DOI: 10.1103/PhysRevB.67.155306.

42 A. Ferrari and J. Robertson, Interpretation of Raman Spectra of Disordered and Amorphous Carbon, *Phys. Rev. B: Condens. Matter Mater. Phys.*, 2000, **61**(20), 14095–14107, DOI: 10.1103/PhysRevB.61.14095.

43 A. C. Ferrari and J. Robertson, Resonant Raman Spectroscopy of Disordered, Amorphous, and Diamondlike Carbon, *Phys. Rev. B: Condens. Matter Mater. Phys.*, 2001, **64**(7), 75414, DOI: 10.1103/PhysRevB.64.075414.

44 K. K. Chinnakutti, S. Thanharaj Salammal, V. Panneerselvam, K. Parasuraman, V. Vishwakarma and D. Ramachandran, Highly Transparent Zinc Nitride Thin Films by RF Magnetron Sputtering with Enhanced Optoelectronic Behavior, *Mater. Sci. Eng., B*, 2018, **232–235**, 33–40, DOI: 10.1016/j.mseb.2018.10.016.

45 A. J. Addie, M. A. Mohammed and R. A. Ismail, Effect of Nitrogen on the Properties of Nanostructured Zinc Nitride Heterojunction Prepared by Reactive Magnetron Sputtering, *Mater. Sci. Semicond. Process.*, 2022, **145**, 106664, DOI: 10.1016/j.mssp.2022.106664.

46 V. B. Shmagin, K. E. Kudryavtsev, D. V. Shengurov and Z. F. Krasilnik, Urbach Absorption Edge in Epitaxial Erbium-Doped Silicon, *J. Appl. Phys.*, 2015, **117**(5), 055303, DOI: 10.1063/1.4907390.

47 P. Wu, T. Tiedje, H. Alimohammadi, V. Bahrami-Yekta, M. Masnadi-Shirazi and C. Wang, Molecular Beam Epitaxy Growth and Optical Properties of Single Crystal Zn3N2 Films, *Semicond. Sci. Technol.*, 2016, **31**(10), 1–4, DOI: 10.1088/0268-1242/31/10/10LT01.

48 N. Jiang, D. G. Georgiev, T. Wen and A. H. Jayatissa, Reactive Radio Frequency Sputtering Deposition and Characterization of Zinc Nitride and Oxynitride Thin Films, *Thin Solid Films*, 2012, **520**(6), 1698–1704, DOI: 10.1016/j.tsf.2011.08.038.

49 W. Du, F. Zong, H. Ma, J. Ma, M. Zhang and X. Feng, Optical Band Gap of Zinc Nitride Films Prepared by Reactive Rf Magnetron Sputtering, *Cryst. Res. Technol.*, 2006, **41**(9), 889–892, DOI: 10.1002/crat.200510689.

50 F. Zong, H. Ma, W. Du, J. Ma, X. Zhang, H. Xiao, F. Ji and C. Xue, Optical Band Gap of Zinc Nitride Films Prepared on Quartz Substrates from a Zinc Nitride Target by Reactive Rf Magnetron Sputtering, *Appl. Surf. Sci.*, 2006, **252**(22), 7983–7986, DOI: 10.1016/j.apsusc.2005.10.006.

51 M. Moun, M. Kumar, M. Garg, R. Pathak and R. Singh, Understanding of MoS2/GaN Heterojunction Diode and Its Photodetection Properties, *Sci. Rep.*, 2018, **8**(1), 11799, DOI: 10.1038/s41598-018-30237-8.

52 A. I. Hassan, I. H. Hammood and A. J. Addie, Broadband Photodetector Based on Co3O4/ZnO/Si Double Heterojunctions: A Morphological and Optoelectronic Study, *Opt. Mater.*, 2024, **148**, 114974, DOI: 10.1016/j.optmat.2024.114974.

53 S. I. Hussein, R. A. Ismail, N. J. Almashhadani and A. J. Addie, Fabrication of High-Performance Nanostructured CsPbI3/Si Perovskite Photodetector by Pulsed Laser Deposition: Challenges and Prospects, *Opt. Mater.*, 2024, **155**, 115890, DOI: 10.1016/j.optmat.2024.115890.

54 A. M. Yahya, E. T. Salim, A. I. Hassan and A. J. Addie, Ag@Graphene Hybrid Plasmonic Nanocomposites by Spray Pyrolysis: Synthesis, Characterization and Improved Properties, *J. Opt.*, 2024, **53**(3), 2537–2549, DOI: 10.1007/s12596-023-01467-5.

55 I. H. Hammood, A. I. Hassan and A. J. Addie, Chemical spray pyrolysis of CO_3O_4 thin films: thickness-dependent structural, electrical and optical properties, *AIP Conf. Proc.*, 2025, **3169**, 050010, DOI: 10.1063/5.0254200.

56 A. M. Yahya, A. I. Hassan, E. T. Salim and A. J. Addie, Tailoring Optical Properties of Graphene through Silver Nanoparticle Incorporation: A Facile Spray Pyrolysis Approach, *AIP Conf. Proc.*, 2025, **3169**(1), 060003, DOI: 10.1063/5.0254202.

57 S. T. Kassim, H. A. Hadi and R. A. Ismail, Fabrication and Characterization of High Photosensitivity CuS/Porous Silicon Heterojunction Photodetector, *Optik*, 2020, **221**, 165339, DOI: 10.1016/j.ijleo.2020.165339.

58 S. Das, K. J. Sarkar, B. Pal, H. Mondal, S. Pal, R. Basori and P. Banerji, SnS2/Si Nanowire Vertical Heterostructure for High Performance Ultra-Low Power Broadband Photodetector with Excellent Detectivity, *J. Appl. Phys.*, 2021, **129**(5), 053105, DOI: 10.1063/5.0032604.

59 H. Mondal, S. K. Ray, P. Chakrabarty, S. Pal, G. Gangopadhyay, S. Das, S. Das and R. Basori, High-Performance Chlorophyll-b/Si Nanowire Heterostructure for Self-Biasing Bioinorganic Hybrid Photodetectors, *ACS Appl. Nano Mater.*, 2021, **4**(6), 5726–5736, DOI: 10.1021/acsanm.1c00517.

60 Y. Xu, H. Shen, J. Zhang, Q. Zhao, Z. Wang, B. Xu and W. Zhang, High-Performance CuS/n-Si Heterojunction Photodetectors Prepared by e-Beam Evaporation of Cu Films as Precursor Layers, *J. Alloys Compd.*, 2021, **884**, 161121, DOI: 10.1016/j.jallcom.2021.161121.

61 S. S. Shaker, R. A. Ismail and D. S. Ahmed, High-Responsivity Heterojunction Photodetector Based on Bi2O3-Decorated MWCNTs Nanostructure Grown on Silicon via Laser Ablation in Liquid, *J. Inorg. Organomet. Polym. Mater.*, 2022, **32**(4), 1381–1388, DOI: 10.1007/s10904-021-02199-4.

62 A. Hasani, M. R. Mohammadzadeh, H. Ghanbari, M. Fawzy, T. D. Silva, A. Abnavi, R. Ahmadi, A. M. Askar, F. Kabir, R. K. N. D. Rajapakse and M. M. Adachi, Self-Powered, Broadband Photodetector Based on Two-Dimensional Tellurium-Silicon Heterojunction, *ACS Omega*, 2022, **7**(51), 48383–48390, DOI: 10.1021/acsomega.2c06589.